JOURNAL OF GUIDANCE, CONTROL, AND DYNAMICS
Vol. 26, No. 5, September–October 2003

Spacecraft Architecture for Disturbance-Free Payload

Nelson Pedreiro*
Lockheed Martin Advanced Technology Center, Palo Alto, California 94304

A novel spacecraft architecture that provides a solution to the combined problems of payload pointing and isolation from spacecraft vibrations is presented. In this architecture, payload and spacecraft are separate bodies that fly in close-proximity formation and interact through noncontact sensors and actuators to achieve precision payload control and isolation from spacecraft disturbances. Vibration isolation is provided down to zero frequency and isolation performance is not limited by sensor characteristics. The proposed concept has far-reaching implications for space missions with stringent pointing control and stability requirements, allowing faster slews and uninterrupted missions during momentum dumping. The applicability of the proposed concept to future missions is discussed. Analysis and simulation results are presented for a large space telescope and provide a first demonstration of the concept. The results show more than two orders of magnitude performance improvement over state-of-the-art pointing and isolation systems.

I. Introduction

CONTROL and motion stability requirements for current and future spaceborne missions are more stringent than ever, as illustrated by the Next Generation Space Telescope[1] (NGST), Space Interferometry Mission[2] (SIM), and Space Based Laser[3] (SBL), among other missions. The technical challenge of meeting these unprecedented pointing and stability requirements is compounded by the size, complexity, and operational environment of proposed systems. For example, on NGST, most of the system operates at cryogenic temperatures where structural damping can be extremely low and the stringent pointing requirements of SBL have to be achieved in the presence of a severe vibration environment caused by the onboard high-energy laser.

The approaches taken to date to address the vibration problem on precision space systems rely primarily in designing a stiff structure, mitigating disturbances at their sources by design and use of isolation systems, and canceling their effects on the system. For example, great effort goes into the design of quiet reaction wheels and wheel isolation systems, structural control, as well as reactionless mechanisms. Active compensation with fast steering mirrors is used to reduce pointing jitter. This approach is not sufficient, nor adequate, for several high-performance systems that are currently being proposed. Relying on stiff structural design for large precision systems results in prohibitive launch costs. Isolating disturbances at the source can be costly and inefficient, especially for systems with various or distributed disturbance sources. Active cancellation of the effects of disturbances is, in general, effective, but is inherently limited by sensor characteristics. Payload isolation is extensively used, but existing active isolation systems are inherently limited by sensor characteristics.[4,5]

A comparison of the Hubble Space Telescope (HST) and NGST highlights important differences with significant impact on the control system and vibration mitigation approach. Although the diameter of the NGST primary mirror is about three times as large as HST's its target mass is significantly less. NGST has to be designed and built for a fraction of the cost of HST. These two factors alone preclude the approach used on HST, which relies on a stiff structural design to mitigate vibration. NGST will operate in an orbit about the second Lagrange point of the sun–Earth system, making service missions unfeasible or very difficult and costly at best. Therefore, the overall system and control architecture has to be inherently robust.

The Terrestrial Planet Finder (TPF) mission currently under a study led by NASA and the Jet Propulsion Laboratory, California Institute of Technology, provides another example of a future mission with control requirements that are beyond the state of the art. Concepts for TPF include structurally connected space interferometers with baselines of up to 100 m, 30-m-diam coronagraphs with extremely stringent requirements of tens of nanoradians pointing, and subnanometer path length and figure control.[6]

In this paper, a novel concept known as spacecraft architecture for disturbance-free payload (DFP) is presented that provides unprecedented control and motion stability for spaceborne systems. In the proposed concept, payload and spacecraft fly in close proximity formation and interact to allow precision payload pointing and isolation from spacecraft vibrations. The DFP system provides vibration isolation down to zero frequency, and isolation performance is not limited by sensor characteristics. The novelty is in the system architecture and, in particular, the architecture of the control system. Implementation requires only mature and flight-proven sensor and actuator technologies. In addition, the required number of sensors and actuators is small; the control logic requires minimum computational power, and the control system is robust. System-level hardware demonstrations have been completed that validate the DFP concept, its implementation, and its performance.[7] The result is a system that offers superior performance, with low cost and high reliability, that is well suited to address the challenges of future precision space systems.

The paper is organized as follows: First, the DFP concept is described, and the system and control architectures are presented. This is followed by system-level analysis and mission suitability study. Next, a dynamics model for a three-dimensional system is described. Finally, results of analysis and simulation are presented for NGST and compared with alternate system architectures. These demonstrate the significant performance improvement afforded by the DFP architecture.

II. DFP Concept and Control Architecture

The DFP provides a system that includes a payload module and a support module (spacecraft) that are preferably mechanically decoupled (Fig. 1). The motion of the payload module is controlled by reacting on the support module using noncontact actuators located between the two modules. The motion of the support module is controlled to follow the payload module using external actuators that react against the surroundings. In this way, no forces or torques are applied between the payload and support modules to achieve relative motion control, that is, the only forces/torques applied between the

Received 13 June 2002; presented as Paper 2002-5029 at the AIAA Guidance, Navigation, and Control Conference, Monterey, CA, 5–8 August 2002; revision received 12 March 2003; accepted for publication 21 March 2003.

*Staff Research Scientist, Precision Pointing and Controls Department; nelson.pedreiro@lmco.com. Senior Member AIAA.

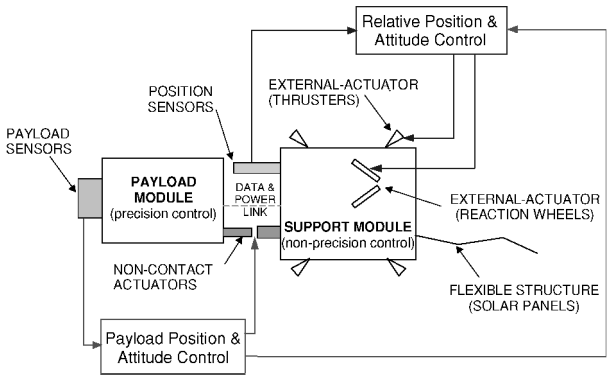

Fig. 1 Spacecraft architecture for DFP, system architecture.

two modules are those required for payload control. This eliminates the inherent conflict between isolation and relative motion control, and vibration isolation is achieved down to zero frequency. Moreover, vibration isolation is not limited by sensor characteristics. In fact, if the sensors used to measure the motion of the payload module with respect to its surroundings, for example, star-tracker and gyros, stopped functioning, the payload module would be adrift, but the support module would continue to follow the payload module and the vibration isolation performance would be unaffected. Similarly, noncontact sensors used to measure the relative motion between the two modules do not affect isolation performance because their signals are used to drive external actuators that do not apply forces on the payload module. In this system, payload and support modules fly in close proximity formation and interact through noncontact actuators to achieve precision motion control and high motion stability of the payload module.

The payload module contains critical components that require precision control and high motion stability, for example, a telescope, a communication system, or a tracking system. The support module contains mission support equipment that does not require precise control and high motion stability. It also contains the main sources of vibration, such as reaction wheels and thrusters, and large flexible appendages, such as solar panels and sunshields. Noncontact position sensors, located between the two modules, are used to obtain information on the relative translation and attitude between the payload and support modules. These sensors can be based on various technologies for noncontact measurement of distance, such as inductive, capacitive, or optical. Noncontact actuators, also located between the payload and support modules, are used to apply forces between the payload and support modules, and to control the motion of the payload module. These actuators can be electromagnetic, such as voice-coil actuators, or electrostatic.

A possible implementation consists of the use of six noncontact position sensors and six noncontact actuators between the payload and support modules in a hexapod configuration. The noncontact actuators are voice-coil actuators, and force control on each actuator allows relative motion between the payload and support modules without transmission of vibrations between the two modules. Force control can be achieved with a high-bandwidth current control loop on the coil assembly of each actuator, which counteracts vibration-induced currents in the coil assembly. External actuators, such as reaction wheels, magnetic torquers, control moment gyros, and/or solar sails, are used to move the support module by reaction against its surroundings, for example, inertial space, and follow the motion of the payload module. Payload or target sensors, such as star-trackers, accelerometers, gyroscopes, and focal plane detectors, provide the information required to control the motion of the payload.

A. Control Architecture

The control architecture for this unique, Lockheed Martin patented system is described next. Figure 2 shows a top-level block diagram of the DFP control system. There are two types of control loops: 1) payload motion control and 2) relative motion control between the payload and the support modules. These two types of control loops are one-way coupled, that is, payload control affects

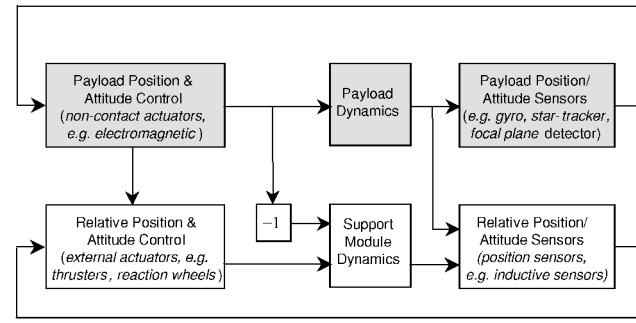

Fig. 2 DFP control system architecture.

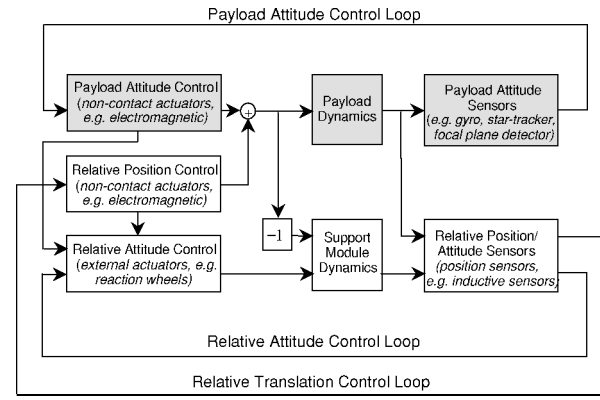

Fig. 3 DFP control architecture with noncontact actuators also used for relative translation control.

relative motion control, but relative control does not affect the payload motion.

Whereas the motion of the payload module is controlled with a high-degree of precision and is very stable, the motion requirements for the support module can be much more relaxed. The support module merely must stay within a sufficient distance and angular range of the payload module to prevent the noncontact position sensors and actuators from going out of range.

A key element of the DFP control architecture is that no forces are applied between the payload and support modules to maintain relative motion control which allows vibration isolation down to zero frequency and isolation that is not limited by sensor characteristics. Another key aspect of DFP is that payload control is achieved by reacting on the support module. Therefore, inertial reacting devices such as reaction wheels or thrusters, which generate mechanical disturbances, are not required on the payload. These represent a significant departure from previously proposed systems such as those described in Refs. 8 and 9. In addition, the DFP control architecture allows the payload to be pointed over the entire celestial sphere.

In applications where some mechanical coupling is required between the payload and support modules, for example, due to data and power cables and/or cooling lines, the noncontact position sensors and noncontact actuators can be used to cancel the effect of the mechanical coupling between the two modules. This represents a simple modification in the control logic and does not require additional hardware. In practice, the cancellation is not perfect and the isolation performance is reduced when compared to an equivalent mechanically decoupled system.

A variation on the described control architecture, shown in Fig. 3, uses the noncontact actuators to perform relative translation control and external actuators to perform relative attitude control between the payload and support modules. In this case, the forces on the noncontact actuators for relative translation control are computed to generate zero moment about the center of mass of the payload module and, therefore, do not affect the attitude of the payload module. This is of particular interest in applications where precise attitude control is required, whereas control of translational motion is less important. In addition, in such applications, the use of external actuators to maintain relative translation control may, in some

cases, present difficulties. For example, the use of thrusters on long-duration missions may require a large amount of propellant that is not feasible to carry onboard the spacecraft.

The architecture shown in Fig. 3 contains three types of control loops: 1) payload attitude control, 2) relative attitude control, and 3) relative translation control. In this case, payload control affects control of both relative attitude and translation, whereas relative attitude control does not affect payload control. This architecture provides zero transmissibility from support module disturbances to payload attitude at all frequencies. In practice, some coupling will occur between the relative translation control and the payload attitude because of errors in the knowledge of the position and orientation of the noncontact actuators with respect to the payload center of mass and because of structural flexibility in the payload. These are implementation issues and not inherent limitations of the proposed architecture.

Note that the payload position and attitude sensors do not have to be physically located on the payload module. This may not be feasible in some applications, in which case the payload position and attitude can be reconstructed from information on the position and attitude of the support module, plus information on the relative position and attitude between the payload and the support modules.

B. Equations of Motion

In the following paragraphs, the equations of motion for the DFP architecture shown in Fig. 2 are presented for the case where the payload and support modules are rigid bodies. Simplifying assumptions are made in this section for discussion purposes that allow the focus to be placed on key aspects of the architecture. A complete formulation, including rigid and flexible body dynamics and large angle motion, was developed and implemented as part of the detailed dynamics model described in Sec. IV. This was used to generate the analysis and simulation results presented in Sec. V.

Consider the two rigid bodies shown in Fig. 4, representing the payload module (PM) and the support module (SM). Let $\boldsymbol{F}_P$ represent the net force acting on the PM, and $\boldsymbol{T}_P^C$ the net torque acting about the PM center of mass. If $\boldsymbol{r}_P$ is the inertial position vector of the center of mass of the PM (CM_P), and $\boldsymbol{M}_P$ is a diagonal matrix with the mass of the PM on the diagonal, then

$$\boldsymbol{M}_P\ddot{\boldsymbol{r}}_P = \boldsymbol{F}_P \tag{1}$$

Let $\boldsymbol{I}_P$ be the central inertia of the PM, that is, inertia about its center of mass. Under the assumption that $\boldsymbol{I}_P$ is constant, and given small angular motion about a nominal orientation and small angular rates, then the attitude of the PM $\boldsymbol{\theta}_P$ is governed by the equation

$$\boldsymbol{I}_P\ddot{\boldsymbol{\theta}}_P = \boldsymbol{T}_P^C \tag{2}$$

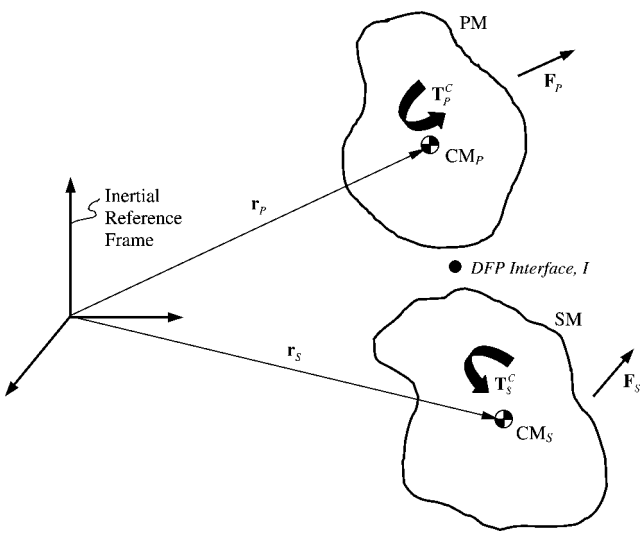

Fig. 4 Free-body diagram for derivation of equations of motion for DFP architecture.

Equations (1) and (2) can be combined for a compact representation of the PM equations of motion,

$$\boldsymbol{\Gamma}_P\ddot{\boldsymbol{X}}_P = \boldsymbol{L}_P^C \tag{3}$$

with $\boldsymbol{\Gamma}_P$, $\boldsymbol{X}_P$, and $\boldsymbol{L}_P$ defined as

$$\Gamma_P \equiv \begin{bmatrix} \boldsymbol{M}_P & \boldsymbol{0} \\ \boldsymbol{0} & \boldsymbol{I}_P \end{bmatrix}, \qquad \boldsymbol{X}_P \equiv \begin{bmatrix} \boldsymbol{\rho}_P \\ \boldsymbol{\theta}_P \end{bmatrix}, \qquad \boldsymbol{L}_P^C \equiv \begin{bmatrix} \boldsymbol{F}_P \\ \boldsymbol{T}_P^C \end{bmatrix} \tag{4}$$

where, for convenience, $\boldsymbol{r}_P$ is replaced by $\boldsymbol{\rho}_P \equiv \boldsymbol{r}_P - \boldsymbol{r}_P^0$, and $\boldsymbol{r}_P^0$ is constant and represents the value of $\boldsymbol{r}_P$ for the system in its nominal configuration. In this way, $\boldsymbol{X}_P$ equals zero in the nominal configuration.

Similar equations can be written for the SM using S as the subscript. By the use of the Laplace transform to express the equations in the frequency domain ($s = j\omega$), the open-loop dynamics of the system consisting of the PM and SM is given by

$$s^2\boldsymbol{\Gamma}_P\boldsymbol{X}_P = \boldsymbol{L}_P^C, \qquad s^2\boldsymbol{\Gamma}_S\boldsymbol{X}_S = \boldsymbol{L}_S^C \tag{5}$$

It is convenient to separate the forces and torques acting on the PM and SM into those acting at the DFP interface, $\boldsymbol{L}_P^I$ and $\boldsymbol{L}_S^I$, and those due to all other sources, $\boldsymbol{E}_P^C$ and $\boldsymbol{E}_S^C$. As before, superscript C indicates forces and torques about the center of mass of each body, and superscript I is introduced to indicate forces and torques at the DFP interface. Forces and torques at the interface can be converted to forces and torques at the center of mass of each body through linear transformations, $\boldsymbol{N}_P$ and $\boldsymbol{N}_S$, respectively, for the PM and SM. With these definitions, and invoking action and reaction at the DFP interface, the forces and torques acting on the PM and SM can be written as

$$\boldsymbol{L}_P^C = \boldsymbol{N}_P\boldsymbol{L}_P^I + \boldsymbol{E}_P^C, \qquad \boldsymbol{L}_S^C = \boldsymbol{N}_S\boldsymbol{L}_S^I + \boldsymbol{E}_S^C, \qquad \boldsymbol{L}_P^I = -\boldsymbol{L}_S^I \tag{6}$$

In the DFP control architecture, only forces and torques required for the control of the PM are applied at the DFP interface, and control of the relative motion between PM and SM is achieved with external actuators that apply forces and torques on the SM. Therefore,

$$\boldsymbol{L}_P^I \equiv -\boldsymbol{K}_P\hat{\boldsymbol{X}}_P = -\boldsymbol{K}_P\boldsymbol{X}_P - \boldsymbol{K}_P\tilde{\boldsymbol{X}}_P$$

$$\boldsymbol{E}_S^C \equiv -\boldsymbol{K}_R\left(\hat{\boldsymbol{X}}_R - \boldsymbol{X}_R^0\right) + \boldsymbol{D}_S^C = -\boldsymbol{K}_R(\boldsymbol{X}_S - \boldsymbol{X}_P) - \boldsymbol{K}_R\tilde{\boldsymbol{X}}_R + \boldsymbol{D}_S^C \tag{7}$$

where $\hat{\boldsymbol{X}}_P$ is the estimate of PM position and attitude, which can be written as the true value $\boldsymbol{X}_P$, plus an estimate error $\tilde{\boldsymbol{X}}_P$, that includes parameter errors and measurement errors such as sensor noise. $\hat{\boldsymbol{X}}_R$ represents the estimate of relative motion between the PM and the SM and can be written as the true relative motion, $\boldsymbol{X}_S - \boldsymbol{X}_P$, plus an estimate error $\tilde{\boldsymbol{X}}_R$. $\boldsymbol{D}_S^C$ represents external disturbances acting on the SM. $\boldsymbol{K}_P$ represents the payload position and attitude control logic and $\boldsymbol{K}_R$ the control logic for relative position and attitude. For example, if proportional–integral–derivative (PID) control is used, then $\boldsymbol{K}_P$ and $\boldsymbol{K}_R$ can be written in the form $\boldsymbol{K} = \boldsymbol{K}^p + (1/s)\boldsymbol{K}^i + s\boldsymbol{K}^d$, where superscripts p, i, and d are used to indicate the PID gain matrices.

The closed-loop equations of motion using the DFP control architecture can be obtained by the substitution of Eqs. (6) and (7) into Eqs. (5):

$$\left(s^2\boldsymbol{\Gamma}_P + \boldsymbol{N}_P\boldsymbol{K}_P\right)\boldsymbol{X}_P = -\boldsymbol{N}_P\boldsymbol{K}_P\tilde{\boldsymbol{X}}_P + \boldsymbol{E}_P^C \tag{8}$$

$$\left(s^2\boldsymbol{\Gamma}_S + \boldsymbol{K}_R\right)\boldsymbol{X}_S = (\boldsymbol{N}_S\boldsymbol{K}_P + \boldsymbol{K}_R)\boldsymbol{X}_P + \boldsymbol{N}_S\boldsymbol{K}_P\tilde{\boldsymbol{X}}_P - \boldsymbol{K}_R\tilde{\boldsymbol{X}}_R + \boldsymbol{D}_S^C \tag{9}$$

Equations (8) and (9) show that disturbances applied on the SM, $\boldsymbol{D}_S^C$, do not affect the motion of the PM, $\boldsymbol{X}_P$. Therefore, PM isolation from disturbances on the SM is achieved over the entire frequency range, down to zero frequency. The equations also illustrate the clear distinction between PM motion control, for example, pointing, and PM isolation. Whereas PM motion control is affected by forces acting on the PM, $\boldsymbol{E}_P^C$, and by PM sensor characteristics, $\tilde{\boldsymbol{X}}_P$, isolation performance does not depend on sensors characteristics. The

relative motion control and, consequently, the motion of the SM, is affected by the motion of the PM, the characteristics of PM motion sensors and of the sensors used to measure relative motion, and by disturbances acting directly on the SM, $\boldsymbol{D}_P^C$. Note that if momentum exchange devices, such as reaction wheels and thrusters, are used as the external actuators on the SM, the equations of motion can still be written in the form of Eqs. (5), and the one-way coupling of the closed-loop dynamics is preserved.

III. Mission Suitability

General characteristics of the DFP architecture and their potential benefits for spaceborne missions are summarized in Table 1. The extent to which the benefits can be realized depends on the specific mission and needs to be evaluated for each case. Nonetheless, for missions where pointing and motion stability requirements are stringent, the benefits can be significant, not only in increased performance, but also in the form of reduced cost, schedule, and risk. In addition, the feasibility of the DFP technology has been established through system-level hardware demonstrations,[7] and its maturity is currently at NASA Technology Readiness Level of 4.

Another benefit of the proposed architecture relates to ground testing of large systems, which are literally divided into two smaller subsystems, PM and SM, with a well-defined interface. These can be tested separately to different sets of requirements.

Potential issues associated with the DFP architecture and possible solutions are listed in Table 2. As indicated, technology exists to address these potential issues, and no issue is considered a fundamental challenge.

Testing the DFP system in a 1-g environment requires offloading, and launch locks are required at the DFP interface. These two items are not issues specific to the DFP system because both are required with the use of any mid- to high-performance isolation system.

The DFP technology has potential applications for any mission with stringent pointing and stability requirements. It is applicable to small and large payloads, and even extreme cases where the payload is significantly more massive than the SM can be accommodated. Sensors and actuators at the DFP interface replace vibration isolation systems at disturbance sources, and, in general, allow relaxing requirements on the SM, including performance and dynamics testing and characterization. Control and dynamics behavior of the PM are virtually independent of the SM, allowing improved performance and providing a clear separation of PM and SM requirements.

The NGST, SBL, SIM, TPF, and Planet Imager (PI) are examples of missions with stringent control and stability requirements that can greatly benefit from the DFP technology. By directly addressing major risks and technological challenges, DFP brings significant benefits and increases the overall probability of success for those missions.

DFP is also a key enabling technology for high-precision formation flying and is readily applicable for systems with multiple payloads that are tracking a common target, such as a segmented mirror or the collectors of an interferometer.

IV. Dynamics Model

A detailed dynamics model and simulation of a generic spacecraft using the DFP architecture was generated to provide a first demonstration of the concept and to assess system performance. Because, for most missions, control of payload attitude is far more important than control of payload absolute position, the discussion will focus on the control architecture shown in Fig. 3, where the noncontact actuators are used for relative translation control.

Figure 5 shows a top-level block diagram of the dynamics model for the control architecture of Fig. 3. The model includes rigid- and flexible-body dynamics for the PM and SM, and, due to the unique nature of the control architecture, the rigid-body dynamics include six degrees of freedom for each module. Gyroscopic effects from the reaction wheels are also included. Elastic deformations at nodes of interest are added to rigid-body components of motion at those nodes to generate total linear and angular displacements at each node. These are used to compute various performance metrics, which are specific to each mission.

Models of sensors and actuators are also included, that is, star-tracker, gyros, noncontact position sensors and actuators at the DFP interface, and reaction wheels. Sensor models include noise, bias,

Table 1 Benefits of the DFP architecture

Characteristics	Benefits
Improved vibration isolation	Improved mission performance Relaxed requirements on spacecraft Use of larger wheels for faster slewing
Uninterrupted mission during momentum dumping	Increased mission throughput Simplified/automated operations
Thermal isolation between payload and spacecraft	Improved payload thermal stability
One-way coupled architecture	Payload insensitive to characteristics of support module, for example, dynamics and microdynamics and fuel slosh Allows reduced testing of spacecraft, for exampe, modal testing
Single point isolation	No need to isolate disturbance at various sources Small number of sensors and actuators
Quasi-independent control of payload and support modules	Control of payload only limited by payload characteristics reduces requirements on modeling and testing of spacecraft
Full control of interface	Robust system accommodates unknown on-orbit effects
Flexible system architecture	Applicable to large class of missions Allows docked operations
Mature sensor and actuator technology	Low-cost, low-risk design

Table 2 Potential issues and possible solutions

Issues	Solutions
Data link between modules	Noncontact data transfer, for example, infrared, wireless Ethernet, or use of cables between payload and support modules
Power transfer between modules	Noncontact power transfer, for example inductive, microwave, or use of cables between payload and support modules, and/or use of batteries on the payload
Maneuvering (slew)	Size noncontact actuators for maneuvering, or to make contact, for example dock or nest for maneuvering
Fail–safe	Use redundant sensors and actuators, and/or dock modules in case of failure, use mechanical stops to limit allowable relative motion

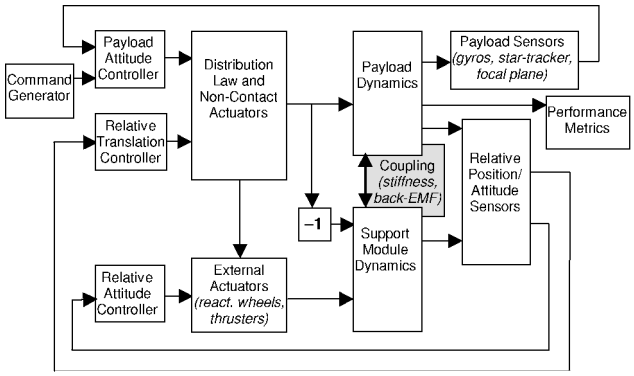

Fig. 5 Top-level block diagram of DFP dynamic model.

drift, nonlinearities, and quantization effects. The reaction wheel model includes disturbances due to wheel drag and various harmonics due to static and dynamic imbalance.

The command generator computes trajectory commands for the various operational scenarios, for example, staring, tracking, slewing, and momentum dumping. These are processed by the control logic, which sends commands to the various actuators, that is, noncontact actuators, reaction wheels, and thrusters. The payload attitude loop consists of feedforward and feedback control logic and uses signals from the payload attitude sensors to compute the torque to be applied to the PM by the noncontact actuators. The relative translation control also consists of feedforward and feedback components and uses an estimate of the relative translation between the two modules to command the noncontact actuators. A distribution law is used to compute the commands to each of six actuators at the DFP interface, in such a way that the net force required for translation control is obtained, whereas it still generates zero torque about the center of mass of the PM. Relative attitude control consists of feedforward, precompensation, and feedback components and is achieved with the reaction wheels.

The feedback and precompensation components of the control logic are used all of the time, whereas the feedforward component is used only during slewing and momentum dumping. PID control is used for implementation of the various control loops. Integrator antiwindup is used to improve performance in the presence of saturation of the noncontact actuators and reaction wheels.

The dynamics model allows the inclusion of various coupling mechanisms, such as stiffness across the DFP interface (due, for example, to data and power cables) and coupling caused by the noncontact actuators, for example, the back-emf effect on electromagnetic actuators. Errors in the knowledge of system parameters, such as mass and inertia properties, geometry, and location and orientation of noncontact actuators also cause coupling and are included in the model.

V. NGST Case Study

The NGST was identified as a mission that could greatly benefit from the DFP architecture, and, therefore, a case study was conducted specifically for NGST. This encompassed layout and preliminary design of the DFP interface, performance assessment, and identification of mission implications. The dynamics model and simulation described in the preceding section were used to assess the performance of the NGST–DFP system and to determine its robustness and sensitivity to various parameters. Performance was compared against that of alternate architectures to gain insight and quantify the improvements provided by the DFP architecture.

The NGST presents a particular challenge due to its configuration, which consists of a PM that is significantly larger and more massive than the SM. Use of DFP in this case means that a PM with larger mass and inertia reacts against a smaller SM. This could potentially drive requirements such as range of motion at the DFP interface and knowledge of system parameters used in feedforward and precompensation portions of the control logic. Because it is more common to have systems where the payload is much smaller than the SM,

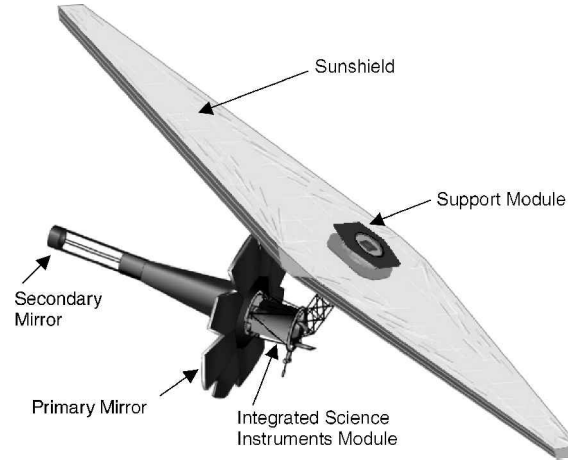

Fig. 6 NASA concept for the NGST.[1]

showing that DFP is suitable for NGST is strong indication that it can be applied to a broad range of missions.

A. NGST Background

Figure 6 shows an illustration of NGST (Ref. 1). Shown in Fig. 6 are the 8-m segmented primary mirror, the secondary mirror, the science instrument module, the support module containing solar panels, reaction wheels, thrusters and other mission support equipment, and the sunshield. For this overall large, complex, lightweight structure, significant portions of which operate at cryogenic temperatures and are subjected to very low disturbance levels, the structural damping is not only expected to be small,[10] but it cannot be predicted with confidence. As a consequence, during a scientific observation, vibrations excited by disturbance sources such as reaction wheels and cryocoolers can be significant and translate directly into degraded image quality. In addition, thruster firings required for stationkeeping and momentum dumping, and slewing maneuvers, can excite significant structural vibrations that take a long time to damp out. This translates directly into a reduction in the time available for conducting scientific observations.

Science requirements flow down into observatory pointing and stability requirements that can be expressed as centroid image motion (jitter) and wave front quality. For NGST, these requirements are 5-mas rms (1 mas $= 10^{-3}$ arcsec) jitter and 140-nm rms wave front error, a portion of which is allocated to the effects of mechanical disturbances. These requirements have to be achieved in the presence of various disturbance sources, of which the reaction wheels have the most significant impact on performance.[11,12]

The control system originally proposed for NGST[1,11] consists of a low-bandwidth, 0.03-Hz, spacecraft attitude control to avoid exciting structural modes. This control system also includes an active image motion compensation system with a 2–6 Hz bandwidth that uses a two-axis steering mirror to correct for centroid image motion. A portion of the near-infrared camera focal plane is used to track a guide star and generate the feedback signal that drives the active image motion compensation loop. This control loop has limited bandwidth due to the integration time required to generate the tracking signal from a faint guide star. This limits the disturbance rejection capability of the image motion compensation loop to low frequencies. Therefore, in this system, it is necessary to limit the disturbance level for frequencies above the bandwidth of the image motion compensation loop. This is achieved by isolating the disturbances at their sources, for example, through a reaction wheel isolation system. This system will be referred to as the conventional system and is one of the systems that will be compared to the DFP architecture.

B. Implementation of DFP for NGST

The proposed implementation of DFP for NGST starts by separating the Optical Telescope Assembly (OTA) and Integrated Science

Table 3 Characteristics of models used for analysis and simulation[a]

DFP	Conventional
Payload module: 1968 kg Support module: 505 kg	Connected system: 2473 kg
DFP actuators used for relative translation control Actuator coupling: $1\ N \cdot m^{-1} \cdot s$	Isolation of disturbances at sources
No active image motion compensation	2-Hz bandwidth active image motion compensation
Hard-mounted reaction wheels	Isolated reaction wheels (1-Hz corner frequency, 40 dB/decade rolloff, 30% damping)
RWA static and dynamic imbalance: $4.1 \times 10^{-6}\ kg \cdot m$ and $1.3 \times 10^{-6}\ kg \cdot m^2$	RWA static and dynamic imbalance: $4.1 \times 10^{-6}\ kg \cdot m$ and $1.3 \times 10^{-6}\ kg \cdot m^2$
Structural dynamics	
62 modes on PM (up to 100 Hz), first mode at 4.5 Hz 155 modes on SM (up to 100 Hz), first mode at 0.4 Hz	214 modes (up to 100 Hz), first mode at 0.37 Hz
0.1% structural damping on all modes PM and SM	0.1% structural damping on all modes
Controls	
Payload attitude control, PID 0.3-Hz bandwidth Relative attitude control, PID 0.03-Hz bandwidth	Attitude control, PID 0.03-Hz bandwidth
Relative translation control, PID 0.03-Hz bandwidth	Assumed ideal reaction wheel isolation with 1-Hz cutoff frequency (40 dB/decade rolloff)

[a]NGST configurations used for performance analysis.

Instrument Module (ISIM) from the spacecraft and sunshield. In DFP nomenclature, the OTA and ISIM form the PM, and the spacecraft plus the sunshield form the SM. This is the preferred arrangement because the OTA/ISIM operate at cryogenic temperatures (~30 K) and have stringent motion and thermal stability requirements. The spacecraft contains the major sources of vibration, such as reaction wheels, gimbaled antennas, thrusters, and fuel slosh and is connected to the sunshield, which has dynamics that are difficult to model and predict and that could couple into the dynamics of the telescope. A cryocooler, if required, should preferably be located on the SM. This favors a design where part of the spacecraft bus is close to the ISIM.

The DFP interface contains six noncontact actuators, six position sensors, launch locks, and mechanical stops to limit the relative motion between the payload and support modules. For NGST, this interface would have a very compact envelope consisting of an annular cylinder with an internal diameter of 0.9 m, external diameter of 1 m, and height of 0.1 m. The interface can also be made modular and inserted between the payload and support modules, for example, on the back of the ISIM, without significant changes on the overall mechanical design.

Computations of required actuator force and range for application on NGST indicate that small voice-coil actuators can be used, with each actuator weighting less than 1 kg. Similarly, cryogenic versions of noncontact position sensors are commercially available that meet range and accuracy requirements for use on NGST.

C. NGST–DFP Dynamics Model

The detailed dynamics model described in the preceding section was used to assess the performance of NGST with the DFP architecture. An existing structural model for the Lockheed Martin NGST design was modified to generate a model for the payload module and a model for the support module (Fig. 7). An optical model was integrated with the simulation to generate a measure of performance in terms of centroid image motion in the focal plane (jitter) and wave front error. The optical model used in the analysis consists of optical sensitivities that relate displacements of various nodes representing optical surfaces to image motion in the focal plane. These sensitivities were obtained by tracing in excess of 1000 rays using an optical analysis program.

Table 3 contains information related to the models used in the analysis and simulations. For comparison, results were also obtained for a connected system with a conventional control architecture,[12] which uses reaction wheel isolation and active image motion compensation through a two-axis fast steering mirror. Note that, on the DFP system, the reaction wheels are hard-mounted, eliminating the need for wheel isolation and the associated launch locks. Active image compensation through fast steering mirrors is not used in the DPP system. This results in approximately the same mass for systems with the conventional and the DFP configurations.

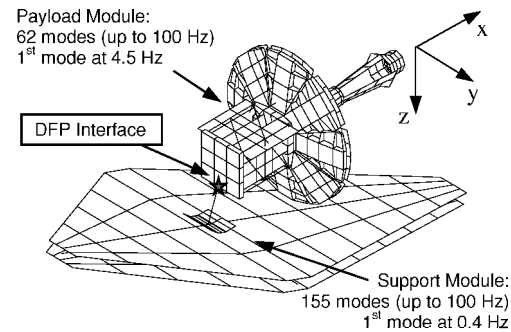

Fig. 7 Structural model used in NGST-DFP analysis and simulation.

Both frequency analysis and time-domain simulations were conducted to assess performance. All structural modes were used in the frequency analysis, whereas modal reduction was used in the simulations to reduce execution time.

Because the reaction wheels were identified as the major sources of disturbances, the analysis focused on their effect on performance. Other disturbance sources are not included, to allow isolation of the effect of the wheels on performance and to assess the relative performance between the conventional system and DFP.

D. Analysis and Performance Results

Figure 8 gives a measure of the isolation performance provided by the DFP architecture. It presents the maximum transmissibility from motion of the SM to motion on the PM. The geometric centers of the DFP interface on the SM and PM were used as reference points for computation of transmissibility. The four curves presented show transmissibility from linear and angular motions on the support module to linear and angular motions on the payload module. Each curve is obtained by computation of the maximum singular value of the corresponding 3×3 transfer function matrix at each frequency point. The results correspond to the DFP control architecture shown in Fig. 5, with no mechanical stiffness across the interface. The effect of actuator coupling is included and reflects the amount of back-emf expected ($1.0\ N \cdot m^{-1} \cdot s$) with existing technology and the voice-coil actuators sized to meet NGST requirements.

The coupling effect due to the relative translation control is clearly seen in Fig. 8a, where the transmissibility from SM linear motion to PM linear motion approaches one for frequencies below the bandwidth of the relative translation control (0.03 Hz). The coupling shown in Figs. 8b and 8d is solely due to the actuator back-emf

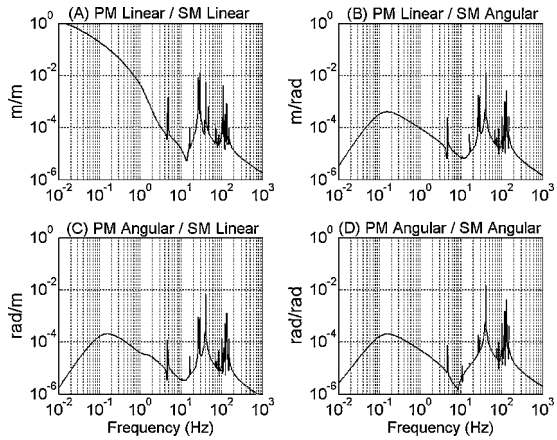

Fig. 8 Maximum transmissibility from SM to PM for the DFP system.

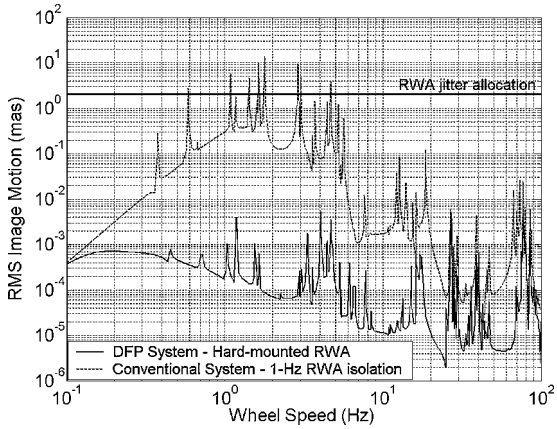

Fig. 9 NGST jitter due to reaction wheel disturbances.

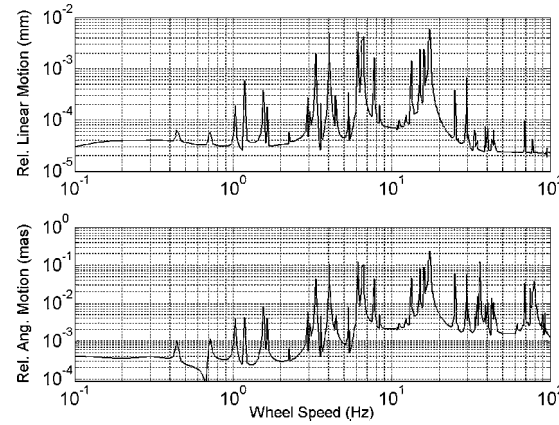

Fig. 10 Relative motion at DFP interface due to reaction wheel disturbances.

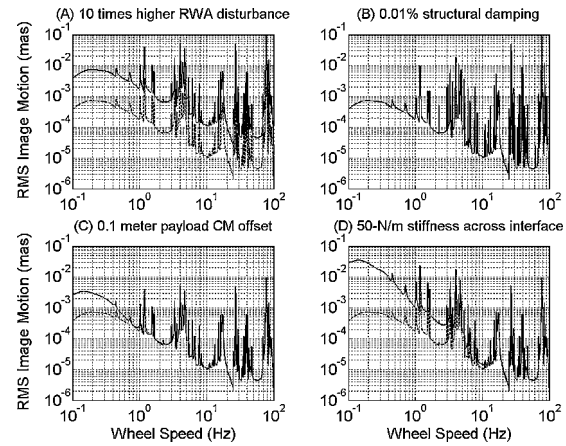

Fig. 11 Effect of various parameters on NGST–DFP jitter due to wheel disturbances.

effect, and the coupling shown in Fig. 8c is caused both by the relative translation control loop and actuator coupling.

Image motion in the focal plane due to reaction wheel disturbances is shown in Fig. 9 for DFP and for the conventional system described in Table 3. The reaction wheel assembly (RWA) consists of four reaction wheels, which are assumed to have the same speed. The 2-mas jitter allocation to RWA disturbances is also shown in Fig. 9. Overall, DFP provides over two orders of magnitude improvement in performance when compared to the conventional system. Moreover, note that the performance of the DFP system meets the 2-mas jitter allocation to wheel disturbances with a significant margin over the entire frequency range. The high performance at low frequencies shows that active image compensation based on a fast steering mirror is not required by the DFP system. The significant performance margin leads directly to lower risk and relaxation of requirements on spacecraft components, such as reaction wheels. Furthermore, part of the error budget allocated to wheel disturbances can be reallocated to other error sources, reducing overall mission risk.

Figure 10 shows the relative motion at the DFP interface due to reaction wheel disturbances during science observation mode. The relative motion at the interface is on the order of 10 μm. Larger relative motions are expected during slewing and momentum dumping due to larger forces at the interface and errors in the knowledge of the system characteristics, such as SM mass properties.

Figure 11 shows the effects of various parameters on jitter performance of the DFP system. In all plots in Fig. 11, the performance of the baseline DFP system (Table 3) is shown as a dashed line for comparison. Figure 11a shows the jitter performance for reaction wheel disturbances that are 10 times higher than the nominal. Figure 11b shows jitter for a system with 10 times less structural damping, that is, 0.01%. Figure 11c shows the effect of an error of 0.1 m in the knowledge of the location of the payload module center of mass. Figure 11d shows the effect of a mechanical connection across the DFP interface with stiffness of 50 N/m.

The results in Fig. 11 clearly show the robustness of the DFP system to changes in the various parameters. Performance with a 10-times increase in wheel disturbance shows that RWA requirements can be greatly relaxed. The result for decreased structural damping is particularly relevant for NGST because the payload module operates at cryogenic temperatures, and structural damping can be extremely low. Error in the knowledge of the location of the payload center of mass causes coupling between relative translation and payload attitude control, but the impact on performance is small, even for a large knowledge error of 0.1 m. Stiffness across the interface will degrade performance, but this is mostly a systems design issue because technology exists for wireless data and power transfer. NGST requires less than 200 W on the PM, and the cable stiffness across the interface can be made significantly less than 50 N/m. Nonetheless, the performance margin remains large even in the presence of the 50 N/m stiffness.

The combined effects of 10 times larger RWA disturbances, 0.01% structural damping, 0.1-m knowledge error in payload center of mass location, and 50 N/m stiffness across the interface are shown in Fig. 12. Maximum jitter is less than 0.1-mas rms, well below the 2-mas allocation.

Figure 13 contains a comparison between DFP and an alternate system architecture that uses dual-stage vibration isolation. The alternate architecture provides a 1-Hz isolation between the PM and the SM with the isolator mounted at the same location as the DFP interface. In addition, the alternate system uses reaction wheel isolation and active image compensation with a 2-Hz bandwidth. Jitter due to reaction wheel disturbances is shown vs wheel speed. Two cases are shown with 1-Hz isolation between PM and SM: 1) 1-Hz

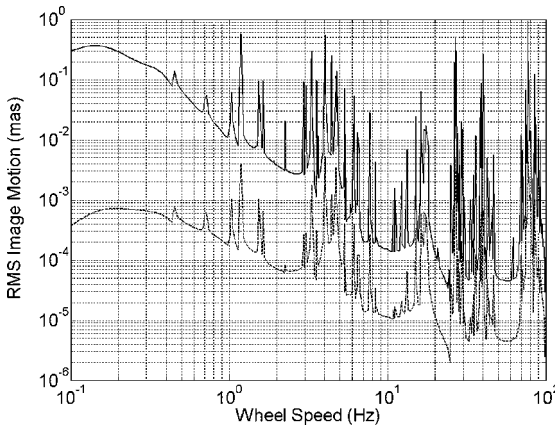

Fig. 12 Jitter for NGST–DFP baseline, ----, and combined effects of 10-times higher RWA disturbance, 0.01% structural damping, 0.1-m PM center of mass offset, and 50-N/m stiffness across the interface, ——.

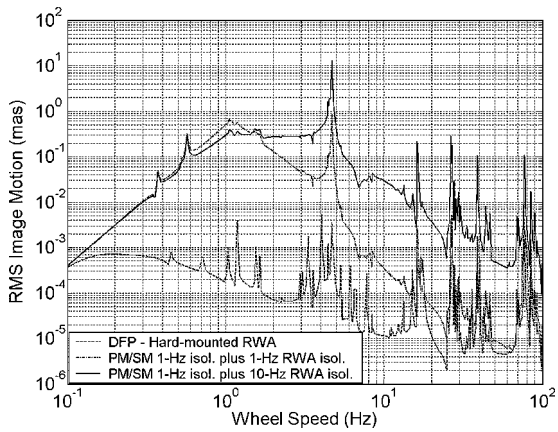

Fig. 13 Comparison of DFP with 1-Hz isolation between PM and SM and RWA isolation.

PM/SM isolation and 1-Hz wheel isolation and 2) 1-Hz PM/SM isolation and 10-Hz wheel isolation. The performance of the dual-stage system between 1 and 2 Hz is limited by the small effectiveness of both the active image compensation and the wheel isolation in this frequency range. The results clearly show the superior performance of the DFP architecture.

The results for the dual-stage isolation system assume ideal isolation with 40 dB/decade rolloff for the wheels and between the PM and SM. Detailed simulations of the RWA mounted on a 1-Hz isolation system have shown considerable motion of the RWA. The observed nutation is expected due to gyroscopic effects of the wheels mounted on a soft suspension system, and this will impact system performance. This effect is not included in the results. Furthermore, as with the DFP system, a 1-Hz reaction wheel isolation system requires gravity offload for ground testing, as well as launch locks.

Comparison of Figs. 11–13 shows that, even in the presence of significantly higher wheel disturbances, lower structural damping, center-of-mass offset, and the specified mechanical link between PM and SM, the performance of the DFP system is superior to the dual-stage isolation system. This demonstrates the robustness of the DFP architecture and the significant performance margins it provides.

In Fig. 14, results are shown for DFP and a dual-stage system, with isolation between the PM and SM that is representative of the state of the art in magnetic isolation[5] with corner frequency of 0.1 Hz and reaction wheel isolation with 10-Hz corner frequency. Similar to DFP, this system does not require a dedicated fast steering mirror for image motion compensation, and it is assumed that the payload attitude is controlled with the same bandwidth used on the

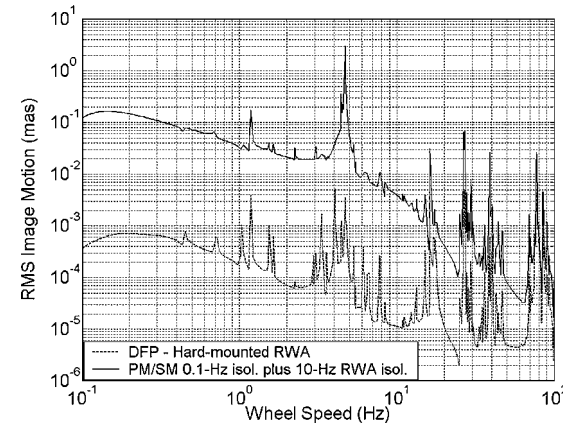

Fig. 14 Comparison of DFP with state-of-the-art magnetic isolation system and RWA isolation.

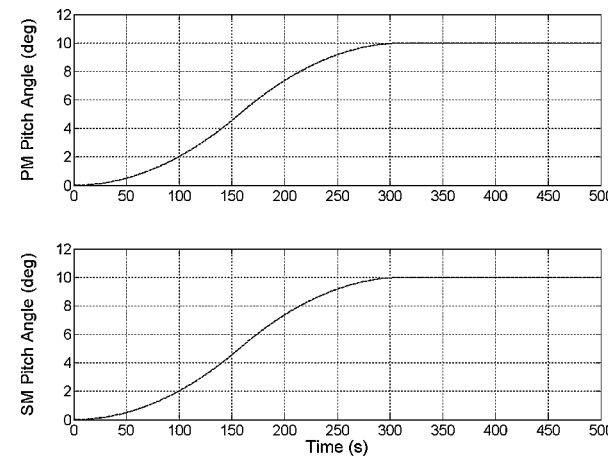

Fig. 15 NGST–DFP 10-deg slew.

DFP system, that is, 0.3 Hz. Although the alternate system meets the requirements over most of the frequency range, the DFP system provides a considerably larger performance margin. As shown in Fig. 14, the change from a very low isolation corner frequency (0.1 Hz) to the zero corner frequency provided by DFP has a significant impact on performance. Isolation down to zero frequency is a unique aspect of the DFP architecture.

E. Slewing and Momentum Dumping

Time-domain simulations were conducted with the NGST–DFP dynamic model to demonstrate capability and assess performance during slewing and momentum dumping. The results presented correspond to the nominal DFP system configuration (Table 3) with no stiffness across the interface. Noncontact actuator coupling is included, as well as five harmonics of RWA disturbances due to static and dynamic imbalance. Sensor noise was not included in the simulations to single out the effect of the RWA disturbances and correlate results from frequency and time-domain analysis. Modal reduction was used, with four modes retained on each module to reduce simulation time. Structural damping of 0.1% was assumed for all modes.

Figures 15–18 show results for a minimum time 10-deg slew about the pitch axis (y axis in Fig. 7). Time histories for the pitch angle of the payload and support modules are shown in Fig. 15. Relative motion at the DFP interface is shown in Fig. 16 and does not exceed 150 μm. Errors in knowledge of system parameters cause control errors and tend to increase the relative motion during slew. A study of the effects of various parameters showed that relative motion of less than 1 mm is expected in the presence of various error sources.

The forces and moments applied at the DFP interface by the noncontact actuators during the 10-deg slew are shown in Fig. 17. These

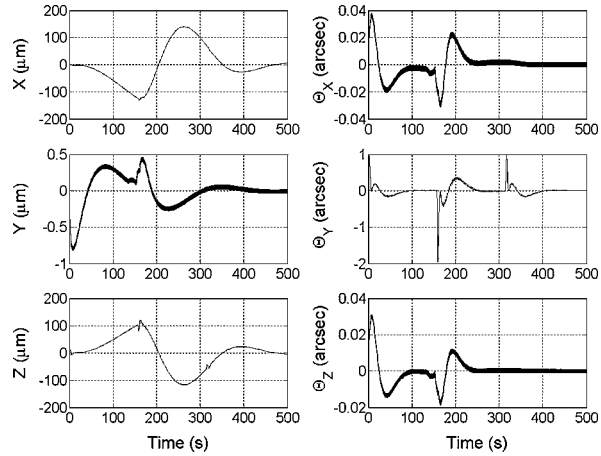

Fig. 16 Relative motion at DFP interface during slew.

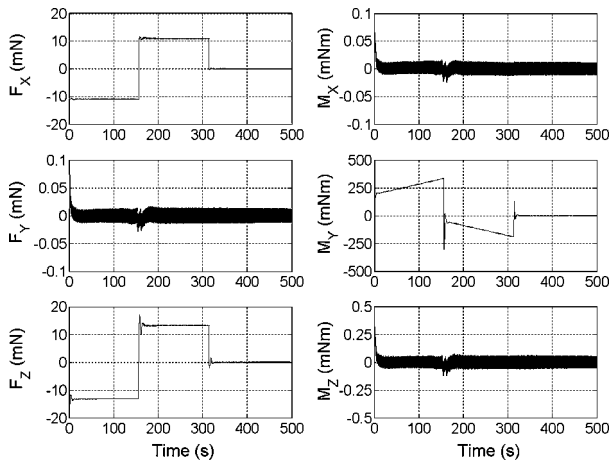

Fig. 17 DFP interface forces/moments during slew.

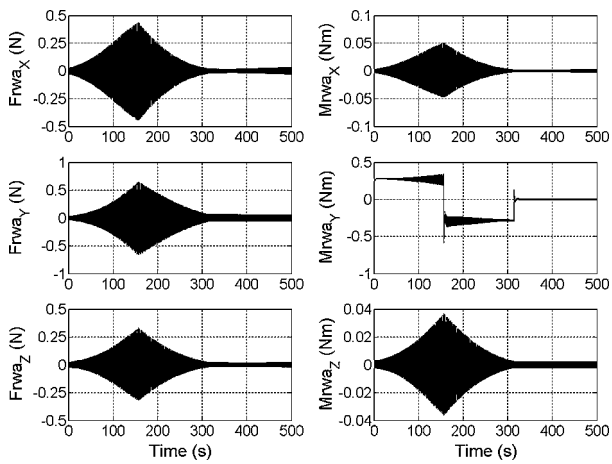

Fig. 18 RWA forces/moments during slew.

drive the force requirement for the noncontact actuators, whereas relative motion at the interface drives the requirements for range of the noncontact position sensors and for the stroke of the noncontact actuators. The results show that actuators with force capability of a fraction of a Newton and stroke on the order of a millimeter will meet the requirements. RWA forces and moments are shown in Fig. 18. The dependency of wheel disturbances on wheel speed can be clearly observed, with the wheels starting at 600 rpm and reaching about 2000 rpm at the midslew point.

The results show fast slew and a settling time that is basically limited by the torque available from the reaction wheels. The time

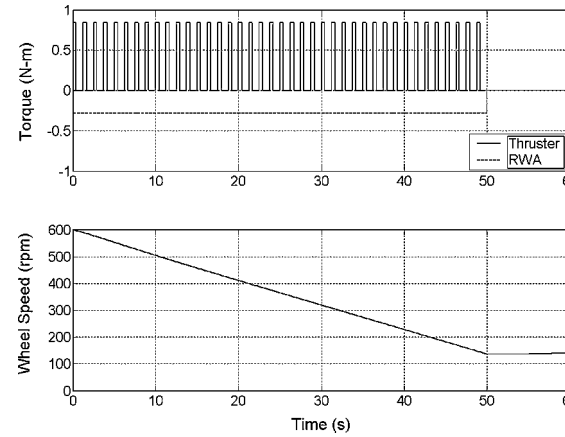

Fig. 19 Thruster and reaction wheel feedforward commands and wheel speed during momentum dumping.

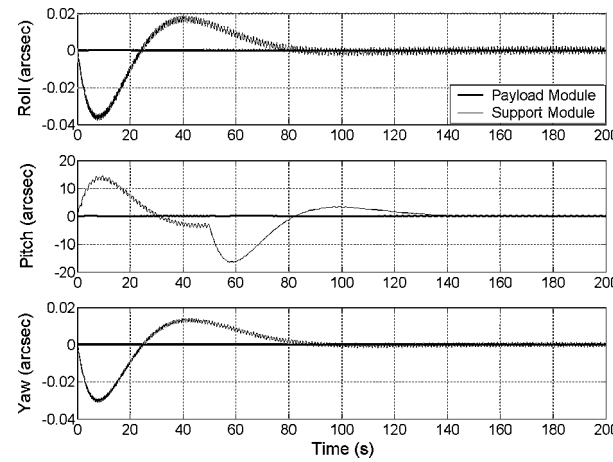

Fig. 20 Roll, pitch, and yaw angles of PM and SM during momentum dumping.

required to settle to a given jitter level depends on the excitation applied to the system, the structural damping, and the frequency of the modes affecting the image motion in the focal plane. By the mechanical separation of the payload from the spacecraft, DFP provides a system for which the modes affecting image quality are at higher frequencies and, therefore, have shorter settling times. For NGST, jitter analysis conducted for the conventional system (connected structure) indicated significant jitter below 10 Hz due to spacecraft-dominated modes exciting mostly rigid-body motion of the payload (OTA/ISIM). This jitter could not be sufficiently reduced by the active image motion compensation (fast-steering mirror) due to its limited bandwidth. This problem is eliminated by DFP.

Momentum dumping results are shown in Figs. 19–23. The torque generated by thruster firings is over three times the torque capability of the RWA, and the thruster duty-cycle was computed accordingly. Figure 19 shows the feedforward commands to the thrusters and RWA, as well as the change in RWA speed. The simulation started with the four wheels at the same speed, about 600 rpm, and momentum was equally dumped on all wheels.

The time histories for PM and SM attitude (Fig. 20) show significant motion of the SM, whereas the payload remains stable. Payload pointing performance during momentum dumping is shown in Fig. 21 in terms of image motion in the focal plane. The maximum value of 0.26 mas is well within the 2-mas allocation due to RWA disturbances, showing that science observations can continue during momentum dumping. This has significant benefits, increasing overall science mission efficiency and allowing automatic momentum dumping, which greatly simplifies mission operations. This is only possible due to the significant isolation provided by DFP.

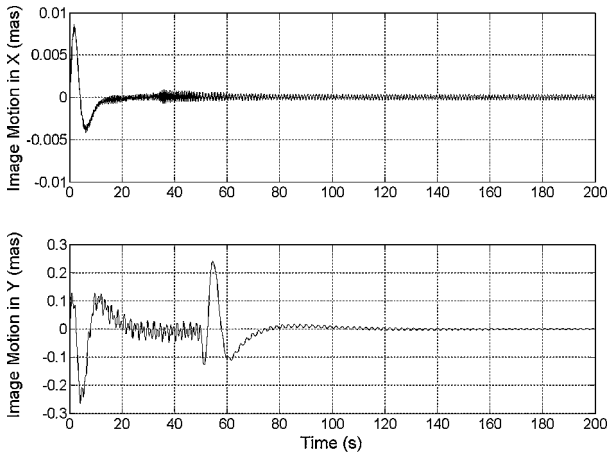

Fig. 21 Image motion in the focal plane during momentum dumping.

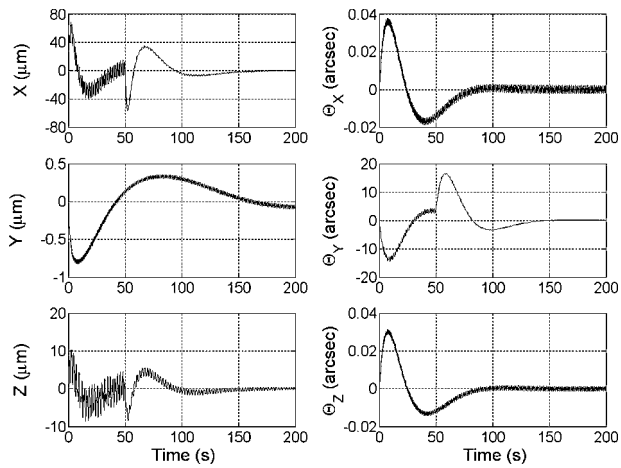

Fig. 22 Relative motion at the DFP interface during momentum dumping.

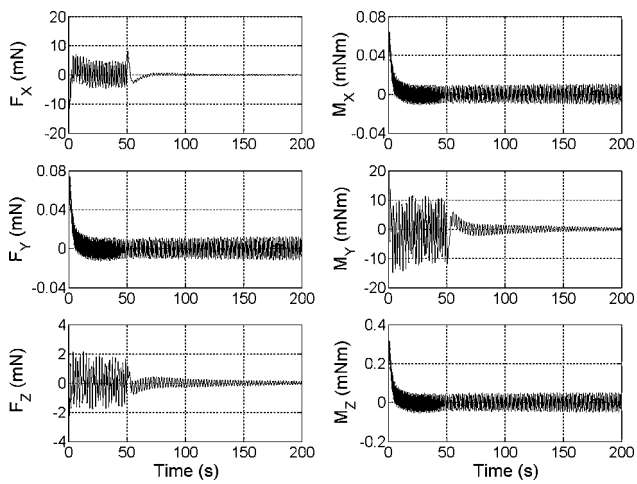

Fig. 23 Forces and moments at the DFP interface during momentum dumping.

Figures 22 and 23 show, respectively, the relative motion and the forces and moments at the DFP interface during momentum dumping. Relative motion is less than 70 μm, and the forces and torques at the interface are approximately 15 mN and 20 mNm, respectively. These are clearly not drivers for the requirements on sensors and actuators at the DFP interface and are well within the capability of existing technology for noncontact position sensors and actuators.[7]

The time-domain simulations demonstrate the slewing and momentum dumping capabilities of the DFP system, as well as key benefits of the DFP architecture, such as fast slewing and settling time and uninterrupted mission during momentum dumping. It also shows that requirements for sensors and actuators can be met with existing technology.

F. Mission Implications

DFP addresses vibration and thermal stability, two key risk areas for NGST. It provides a system that is robust and largely insensitive to disturbances and dynamics of the spacecraft and sunshield, reducing risks both in orbit and for ground testing. This also allows reduction in cost and schedule due to reduced and simplified ground testing and characterization. An increase in science observation time is possible due to shorter slew/settling time and the ability to continue science observations through momentum dumping operations. The large performance margins provided by DFP translate into relaxed requirements for the spacecraft and several components, resulting in a reduction in cost. For example, requirements on reaction wheel balancing are greatly reduced, leading to lower cost. Also, there is no need for a fast-steering mirror, which results in a reduction in cost associated with the components, but mostly with its integration and testing on the overall system. Although some of these benefits are specific to NGST, most are applicable and relevant to any mission with stringent pointing and stability requirements.

VI. Conclusions

A novel system is presented that allows unprecedented control and motion stability for spaceborne payloads. The proposed DFP control architecture overcomes the inherent limitations of existing pointing control and isolation systems, providing vibration isolation down to zero frequency and isolation performance that is not limited by sensor characteristics. In the DFP system, payload and spacecraft fly in close proximity formation and interact to provide control of the payload and simultaneous isolation from spacecraft vibrations.

A detailed dynamics model and simulation were created and used to provide a first demonstration of the DFP control architecture. Analysis and results are presented for the NGST and compared with those of alternate control architectures. It is shown that the DFP system provides isolation performance that is improved by over two orders of magnitude when compared to the state of the art. Slewing capability and the ability to continue the mission during momentum dumping are also demonstrated. The dynamics model was used to assess the effect of various parameters on system performance and to demonstrate the robustness of the DFP architecture.

The DFP concept is applicable to a broad range of space missions with stringent control and motion stability requirements. It has far reaching implications beyond improved performance, such as relaxed spacecraft requirements, simplified on-orbit operations, and reduced requirements for ground testing and characterization. These translate to reduced risk and cost and enable current and future precision space systems.

Acknowledgment

This work was conducted from April to September 1999 under a Lockheed Martin Independent Research and Development Program.

References

[1]Bely, P.-Y., "NGST Yardstick Mission," *Proceedings of the 34th Liege International Astrophysics Colloquium*, ESA Publications, Liege, Belgium, 1998, pp. 159–166.

[2]Lee, A. Y., Yu, J. W., Kahn, P. B., and Stoller, R. L., "Preliminary Spacecraft Pointing Requirements Error Budgets for the Space Interferometry Mission," *IEEE Aerospace Applications Conference Proceedings*, Vol. 4, IEEE Publications, Piscataway, NJ, 1999, pp. 35–47.

[3]Bell, K. D., Powers, M. K., Griffin, S., and Huybrechts, S., "Air Force Research Laboratory's Technology Programs Addressing Deployable Space Optical Systems," *SPIE Conference on Space Telescopes and Instruments*, Vol. 3356, Society of Photo-Optical Instrumentation Engineers, Bellingham, WA, 1998, pp. 535–551.

[4]Lubomski, J. F., Grodsinsky, C. M., Logsdon, K. A., Rhon, D. A., and Ramachandaran, N., "Final Report—Vibration Isolation Technology (VIT) ADT Project," NASA TM 106496, March 1994.

[5]Edberg, D., Boucher, R., Schenck, D., Nurre, G., Whorton, M., Kim, Y., and Alhorn, D., "Results from the STABLE Microgravity Vibration Isolation Flight Experiment," *Advances in the Astronautical Sciences, Guidance and Control*, Vol. 92, Univelt, San Diego, CA, 1996, pp. 567–581.

[6]Beichman, C. A., Coulter, D., Lindensmith, C., and Lawson, P. (eds.), "Summary Report on Architecture Studies for the Terrestrial Planet Finder," Jet Propulsion Lab., California Inst. of Technology, JPL Publication 02-011, June 2002.

[7]Pedreiro, N., Carrier, A. C., Lorell, K. R., Roth, D. E., Shelef, G., Clappier, R., and Gonzales, M., "Disturbance-Free Payload Concept Demonstration," AIAA Paper 02-5027, Aug. 2002.

[8]Laskin, R. A., and Sirlin, S. W., "Future Payload Isolation and Pointing System Technology," *Journal of Guidance, Control, and Dynamics*, Vol. 9, No. 4, 1986, pp. 469–477.

[9]Collins, S. A., and von Flotow, A. H., "Active Vibration Isolation for Spacecraft," International Astronautical Federation, Paper IAF-91-289, Oct. 1991.

[10]Katterloher, R., "Low Temperature Decay of Vibrational Resonance for Bars Made of DISPAL2, Sintered Al-Powder, Alloy MIC-6 and AlMgSil," *Proceedings of the 12th International Cryogenic Engineering Conference*, International Cryogenic Engineering Committee, Grenoble, France, 1988, pp. 455–459.

[11]Mosier, G., Ferniano, M., Ha, K., Bely, P., Burg, R., Redding, D., Kissil, A., Rakoczy, J., and Craig, L., "Fine Pointing Control for a Next Generation Space Telescope," *SPIE Conference on Space Telescopes and Instruments*, Vol. 3356, Society of Photo-Optical Instrumentation Engineers, Bellingham, WA, 1998, pp. 1070–1077.

[12]Pedreiro, N., "Next Generation Space Telescope Pointing Stability," AIAA Paper 2000-4543, 2000.